PNAS
www.pnas.org

Supplementary information for

"Intrinsic planar polarity mechanisms influence the position-dependent regulation of synapse properties in inner hair cells"

Philippe Jean[1,2,3,4], Özge Demet Özçete[1,2,4,5], Basile Tarchini[6,7,8,§] and Tobias Moser[1,2,4,9§]

[§] **Correspondence should be addressed to:**

T. Moser

Institute for Auditory Neuroscience and InnerEarLab, University of Göttingen Medical Center, 37099 Göttingen, Germany

Tel.: +49-551-3922803, Email: tmoser@gwdg.de

or:

B. Tarchini

The Jackson Laboratory, Bar Harbor, ME 04609, USA
Tel. : +1-207-288-6986, Email: basile.tarchini@jax.org

This PDF file includes:

Supplementary text: Materials and Methods

Figs. S1 to S6

References for SI reference citations

Supplementary Information Text

Materials and Methods.

Animals

The Cre-inducible PTXa allele at the *Rosa26* locus and the LGN KO mice have been previously described (1, 2). *Myo15*^{sh2} (JR#109) and *Atoh1-Cre (JR#11104)* (3) were obtained from The Jackson Laboratory. The *Gαi3* mutant strain was derived by breeding from the *Gαi1; Gαi3* double mutant strain obtained from The Jackson Laboratory (JR#24525) (4). The *Gαi2* mutant strain was generated with CRISPR/Cas9 and carries a deletion of *Gαi2* exons 2-4.

Patch-clamp recordings

The apical 2/3 turns of organs of Corti from P21-26 old mice were freshly dissected in HEPES Hank´s solution containing (in mM): 5.36 KCl, 141.7 NaCl, 10 HEPES, 0.5 $MgSO_4$-$7H_2O$, 1 $MgCl_2$-$6H_2O$, 1 mg/ml D-glucose, and 0.5 mg/ml L-glutamine (pH 7.2, ~300 mOsm). The native morphologies and positions of the IHCs within the organ of Corti were maintained as much as possible by accessing them from the modiolus. Patch pipettes were made from GB150F-8P or GB150-8P borosilicate glass capillaries for whole cell and perforated patch-clamp recordings, respectively (Science Products, Hofheim, Germany). All experiments were conducted at room temperature (20-25°C). For whole cell recordings, the patch pipette solution contained (in mM): 111 L-glutamate, 1 $MgCl_2$, 1 $CaCl_2$, 10 EGTA, 13 TEA-Cl, 20 HEPES, 4 Mg-ATP, 0.3 Na-GTP and 1 L-Glutathione (pH 7.3, ~290 mOsm). Perforated patch-clamp experiments were done as

described previously (5). The patch pipette solution contained (in mM): 130 Cs-gluconate, 10 TEA-Cl, 10 4-AP, 10 HEPES, 1 $MgCl_2$, as well as 300 mg/ml amphotericin B (pH 7.17, ~290 mOsm). The extracellular solution contained the following (in mM): 2.8 KCl, 102 NaCl, 10 HEPES, 1 $CsCl_2$, 1 $MgCl_2$, 35 TEA-Cl, 2 mg/ml D-Glucose and either 5 $CaCl_2$ or 1.3 $CaCl_2$ for whole cell and perforated patch-clamp configuration, respectively (pH 7.2, ~300 mOsm). Membrane capacitance measurements in Fig. 4. F-H were done with 100 nM apamin in the extracellular solution. An EPC-10 USB amplifier (HEKA, Lambrecht/Pfalz, Germany) controlled by PatchMaster software (HEKA) was used for the acquisition. IHCs were held at -87 mV after liquid junction potential correction. All voltages were corrected offline for liquid junction potential (-17 mV) and voltage-drops across the series resistance (R_s). For whole-cell recordings, recordings were discarded when the leak current exceeded -50 pA at -87mV, R_s exceeded 15 MΩ within 4 min after break-in, or Ca^{2+}-current rundown exceeded 25%. The membrane capacitance were performed using the Lindau-Neher technique (6). For capacitance measurements, only traces with the leak current lower than -40 pA and R_s lower than 30 MΩ were used for further analysis. In one data set, IHCs were depolarized from the holding potential of -87 mV to -17 mV for durations of 2 ms to 50 ms and in another one to different voltage range from -53 mV to -37 mV with 2 mV increments for 100 ms, in order to probe weak depolarizations, with 20 s interval, in each case.

Spinning disk microscopy and live confocal Ca^{2+} imaging

Ca^{2+}-imaging was performed with a spinning disk confocal scanner (CSU22, Yokogawa, Germany) mounted on an upright microscope (Axio Examiner, Zeiss, Germany) with 63x, 1.0 NA objective (W Plan-Apochromat, Zeiss). The spinning disk was set to 2000 rpm to synchronize with the 100 Hz acquisition rate of the camera to avoid the uneven illumination. Images were acquired by a scientific CMOS camera (Neo, Andor, Northern Ireland), with a pixel size of 103 nm. To visualize the Ca^{2+}-hotspots and the ribbons, the low affinity Ca^{2+}-indicator Fluo-4FF penta-K^+ salt (0.8 mM, Life Techologies, Germany) and the TAMRA-conjugated CtBP2/RIBEYE-binding dimer peptide (10 µM, Biosynthan, Germany) were added to the

intracellular solution just before experiment. The Ca^{2+}-indicator Fluo-4FF was excited by the 491 nm diode-pump solid-state (DPSS) laser (Calypso, Cobolt AB, Solna, Sweden), and the red fluorescence from TAMRA was excited by the 561 nm DPSS laser (Jive, Cobolt AB). Using a piezo positioner for the objective (Piezosystem, Germany), a scan of the entire cell was performed 4 min after breaking into the cell, taking sections each 0.5 µm at an exposure time of 0.5 s in the red (TAMRA-peptide) channel from the bottom to the top of the cell. In order to study the voltage-dependence of Ca^{2+}-indicator fluorescence increments at the synapses, the confocal scans were acquired every 0.5 µm from the bottom-most to the top-most ribbon. Ca^{2+}-currents were evoked by applying a voltage ramp stimulus from -87 to +63 mV during 150 ms (1 mV/ms) in each focal plane. Simultaneously, fluorescence measurements were made in the green channel (Fluo-4FF) with a frame rate of 100 Hz. In order to overcome the limitations of the frame rate and increase the voltage resolution of the fluorescent signal acquired, the voltage ramp protocol was applied twice, once shifted by 5 ms such that for any given frame during the second ramp the voltage was shifted by 5 mV compared to the first stimulus. The interval between 2 sequential sections was 2 s to avoid Ca^{2+} dependent inactivation of Ca^{2+}-channels. Alternating planes were acquired to avoid photobleaching encountered with the consecutive plane acquisitions.

Immunohistochemistry, confocal and high resolution STED imaging

The samples were fixed in formaldehyde (4%, 10 min to 1h on ice depending on the antibodies). Afterwards, the following primary antibodies were used: mouse anti-CtBP2 (1:200, BD Biosciences, 612044), mouse anti-PSD-95 (1:200, Sigma Aldrich, P246-100ul), rabbit anti-Cav1.3 (1:100, Alomone Labs, ACC 005), rabbit anti Vglut3 (1/300, Synaptic Systems, Germany, 135 203), guinea-pig anti Vglut 3 (1/300, Synaptic Systems, Germany, 135 204), rabbit anti- otoferlin (1:100, Cedarlane/Synaptic Systems 178003(SY)), rabbit anti-KCNMA1 (BK) (1:200, Alomone Labs, APC 021). Secondary antibodies used were Alexa Fluor 488 conjugated anti-rabbit, Alexa Fluor 488 conjugated anti-guinea-pig, Alexa Fluor 568 conjugated anti-mouse, and Alexa Fluor 647 conjugated anti-rabbit (1:200, Invitrogen, A11008, A11073

A11004, A31573 respectively). For high resolution STED microscopy, STAR580 and STAR635p conjugated anti-mouse and rabbit respectively (1:200, Abberior, Germany, 2-0002-005-1 and 2-0012-007-2 respectively) have been used as secondary antibodies. Images were acquired using a Zeiss LSM800 or an Abberior Instruments Expert Line STED microscope, with excitation lasers at 488, 561, and 633 nm and STED lasers at 775 nm, 1.2 W, using a 1.4 NA 100x oil immersion objective, either in confocal or in 2D-STED mode. Images were adjusted for brightness and contrast using Image J.

Data analysis

Live-imaging and IHC-patch-clamp

The data were analyzed using custom programs in Igor Pro 6.3 (Wavemetrics, Portland, OR, USA). For analysis of IV-curves, the evoked Ca^{2+}-currents were averaged from 5 to 10 ms after the start of the depolarization. ΔF images were created by subtracting the fluorescence intensities inside the cell at resting state (F_0, average of 10 frames) from the ones at the depolarized state (average of 6 frames during voltage ramp protocol). ΔF for each hotspot was calculated as the average of a 9 pixel square placed in the region exhibiting the greatest intensity increase within the fluorescent hotspot. The fluorescence-voltage relationship (FV) was sorted by the corresponding voltage of each fluorescence intensity value. Maximal ΔF (ΔF_{max}) was the average of 5 ΔF values obtained during the voltage ramp protocol (at the peak of Ca^{2+} influx). Only fluorescent increments presenting a ΔF_{max} greater than the average of the fluorescence intensity plus 2 standard deviations at rest were defined as synaptic Ca^{2+} signals and considered for further analysis. Due to their variance, analysis of their voltage dependence was performed on fits to the raw FV traces using the following function:

$$F(V) = F_0 + \frac{f_v \cdot (V_r - V)}{1 + e^{\frac{(V_h - V)}{k}}}$$

where V stands for the voltage command. The fitting parameters were determined by Igor Pro automatically, and their initial guess resulted from the estimations of F_0, the signal at rest, V_h for the voltage value of half-maximal activation and k for the voltage sensitivity obtained from a sigmoid fitting. The slope factor f_v was obtained by linear fitting of the FV-trace in the range of 3 to 23 mV, where the decrease of fluorescence at positive voltages results from the declining driving force despite full activation of the Ca^{2+} channels. The resulting fitting trace was forced to reach the reversal potential V_r, obtained from the corresponding whole-cell Ca^{2+}-currents. The FV fit was then divided by the f_v. line extrapolated to all the corresponding voltages, to estimate the hotspot fractional activation curves. The fractional activation curves were then fitted by the Boltzmann function to obtain the voltage for half activation (V_h) and slope-factor (k).

Synaptic ribbon fluorescence (visualized with the TAMRA-conjugated CtBP2/RIBEYE-binding dimer peptide) was estimated by measuring the ratio of the strongest fluorescence pixel intensity to that of the pixel nearby the hotspot (8-9 pixels away inside the cell) (F_{ribbon}/F_{nearby}). The spatial extent of the synaptic Ca^{2+}-signals was estimated by fitting of a 2D Gaussian function to the fluorescent hotspot using a genetic fit algorithm (7) to obtain the full width at half maximum in the long and short axis. For each spot, the calculations were made at those confocal sections where the intensity of the spot was strongest.

In order to combine live-imaging data from multiple cells, we reconstructed the morphology of individual IHCs and the positions of their synapses based on the fluorescence of the TAMRA-conjugated RIBEYE-binding peptide and then transformed the Cartesian coordinates into cell-aligned cylindrical coordinates (for more details see (8)). In brief, for each cell we identified the plane of symmetry orthogonal to the tonotopic axis. Then we sectioned the IHC orthogonally to a straight line fitting the pillar edge of

the cell in the plane of symmetry. We calculated the center of mass for each section and connected those of the bottom-most and of the largest section to define the central axis for our cylindrical coordinate system. We projected the AZ coordinates of multiple cells along their central axis for the polar charts, with the 4 sides annotated as modiolar or pillar (facing toward or away from the ganglion), and apical or basal (toward the cochlear tonotopic apex or base).

Immunostaining

Confocal and STED immunofluorescence images were analyzed and z-projected with Fiji software and further analyzed using Igor Pro. The spatial extents of the Ca^{2+}-channel clusters and PSD-95 was estimated in 2D STED images by assessing the full width at half maximum in the long and short axis by fitting a 2D Gaussian function (7). The intensities of the spots were estimated by taking the amplitude of the Gaussian fits at the confocal level. The position-dependent intensity of the ribbons was analyzed by a customized algorithm in MATLAB software and used as a plug-in in Imaris. The positions of the ribbons were defined as the centers of mass of CtBP2-immunofluorescent spots. The spots were subjectively selected by thresholding the quality of a 3D Gaussian fitting, including or excluding spots. Immunofluorescence intensities were measured as the sum of the voxel values within a defined region (3 voxels in X, Y, and 2 in Z) with the center of mass of the spot as origin. The cytosolic staining allowed to assign each ribbon to an IHC and to properly place the vectors. After marking the center of each IHC nucleus, a vector passing by this point and defining the central axis of the cylindrical model of the cell was adjusted to the relative orientation of each IHC cell in the XY and YZ axis. The Cartesian coordinates of the ribbons were transformed to cell-centric cylindrical coordinates in order to adjust differences in cellular orientation relative to the XYZ axes of the microscope. Multiple cells were then plotted by overlaying their central axes with alignment to the center of each nucleus.

Statistical analysis:

The data were analyzed using Matlab (Mathworks), Igor Pro 6 (Wavemetrics), Imaris 7.6.5 (Bitplane) and Python. Averages were expressed as mean ± standard error of the mean (S.E.M.). For every dataset, the standard deviation (S.D.), number of replicates (n) and animals (N) were indicated. In order to compare two samples, data sets were tested for normal distribution (Jarque-Bera test) and equality of variances (F-test), followed by two-tailed unpaired Student's t-test, or, when data were not normally distributed and/or variance was unequal between samples, the unpaired two-tailed Mann-Whitney-Wilcoxon test was used. The non-significant difference between samples is reported as *n.s.*, significant differences are reported as * $P < 0.05$, ** $P < 0.01$, *** $P < 0.001$, **** $P < 0.0001$.

Supplemental Figures

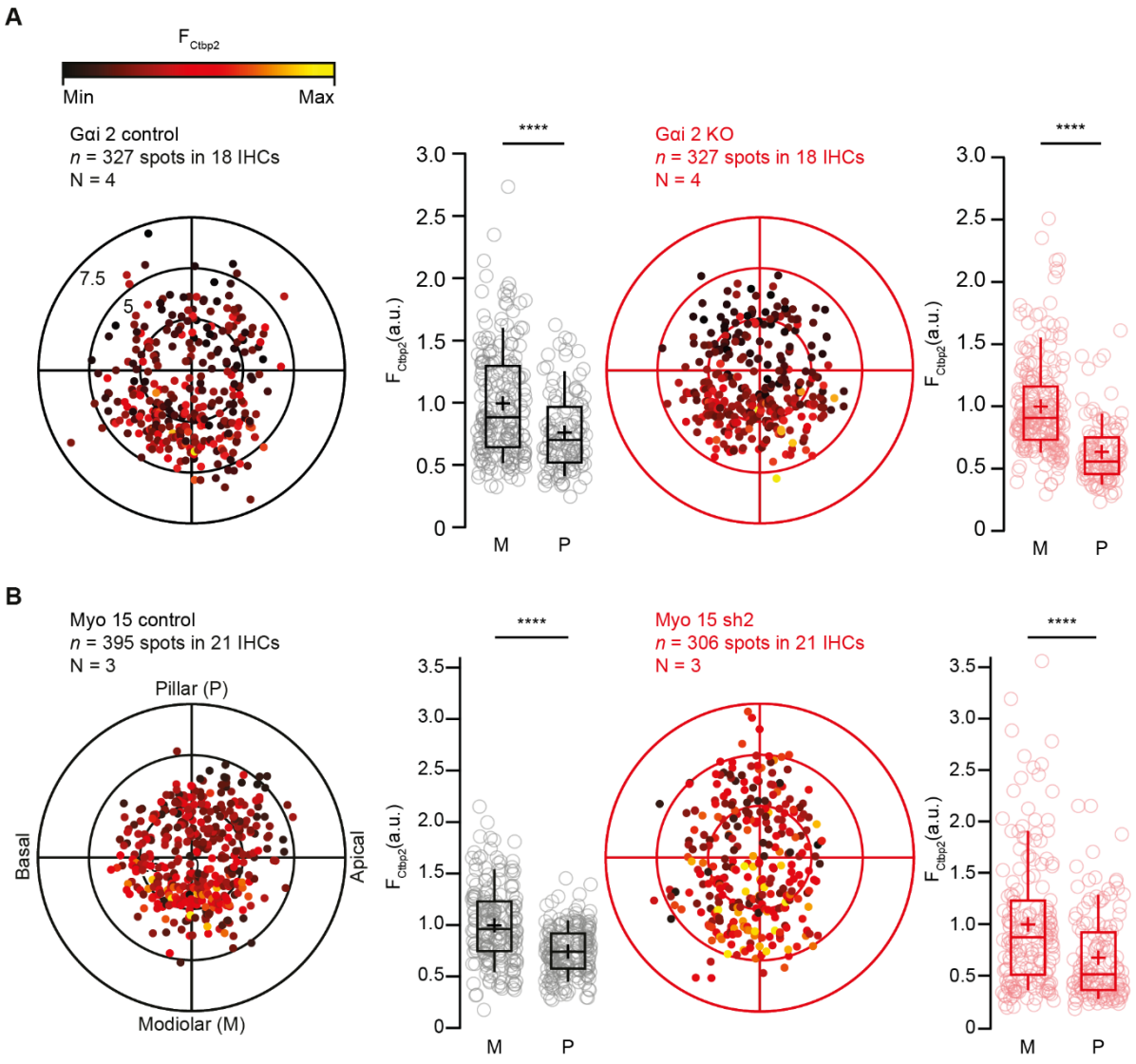

Fig. S1: *Myo15*^{sh2} and *Gαi2*^{KO} mice retain a modiolar-pillar gradient for ribbon size

(A) The polar charts display locations and intensities of immunofluorescently labelled CtBP2 marking the ribbons. Modiolar and pillar refer to facing towards or away from the ganglion in the modiolus, apical and basal refer to the tonotopic axis of the organ of Corti. The fluorescence intensity of each CtBP2 signal point is reflected by its color, with warmer, yellow tones indicating higher intensity, and cooler, darker tones indicating lower intensity. Each radial circle is 2.5 µm. The IHCs from both *Gαi* controls *(Gαi2*$^{+/+}$ or *Gαi2*$^{KO/+}$) and *mutant (Gαi2*$^{KO/KO}$) conditions display a significant modiolar (M)–pillar (P) gradient of ribbon strength (*Gαi2 control* (black): modiolar: n = 213 AZs vs. pillar: n = 114 AZs, *Gαi2*$^{KO/KO}$ (red): modiolar: n = 220 AZs vs. pillar: n = 107 AZs, $p < 0.00001$, Mann-Whitney-Wilcoxon test for both conditions) **(B)** The IHCs from both *Myo15* control (*Myo15*$^{sh2/+}$) and Myo15 mutant conditions (*Myo15*$^{sh2/sh2}$) display a significant gradient of stronger ribbons in the modiolus (M) as compared to the pillar side (P) (Myo15 control (black): modiolar:

n = 203 AZs vs Pillar: *n* = 193 AZs, Myo15 mutant (red): modiolar: *n* = 173 AZs vs Pillar: *n* = 133 AZs, *p* < 0.00001 Mann-Whitney-Wilcoxon test for both conditions).

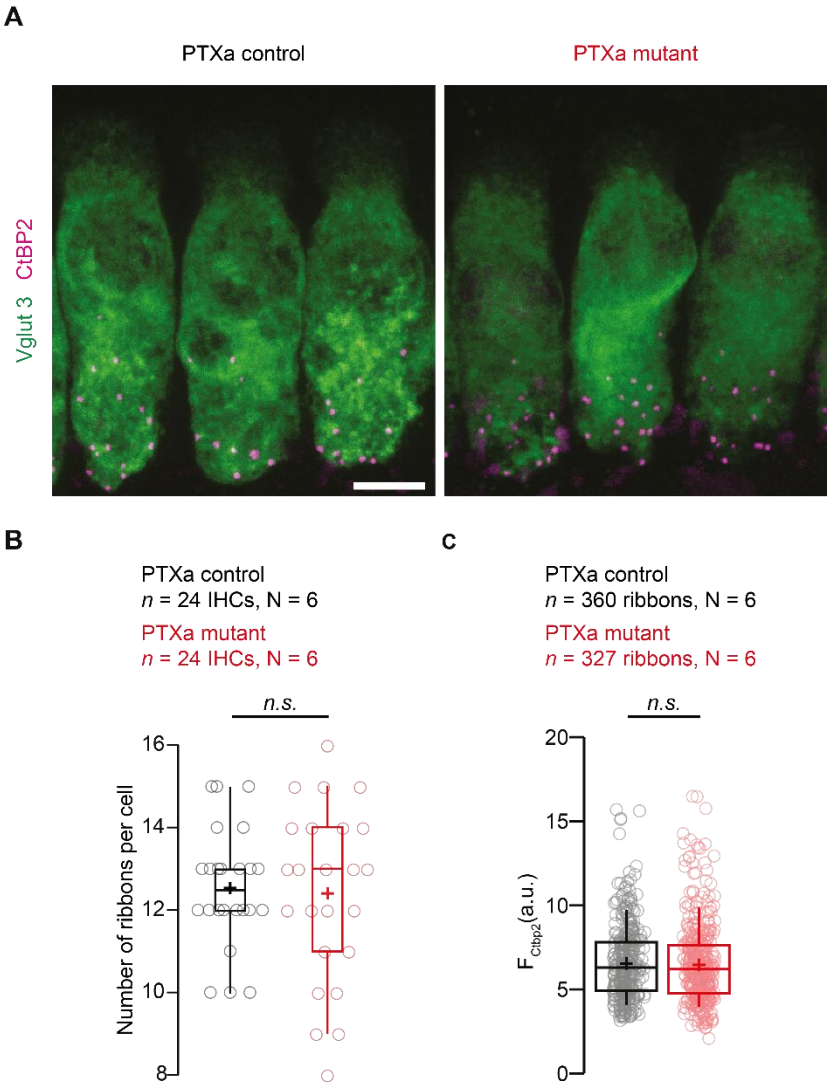

Fig. S2: Disruption of Gαi signaling does not change ribbon size and number

(A) Maximal projection of confocal sections from PTXa control and mutant organs of Corti co-immunolabeled for the IHC marker Vglut3 (green) and the ribbon marker CtBP2 (magenta). Scale bar = 5 µm. **(B)** The average number of ribbons per cell is comparable between PTXa control and mutant conditions (*n* = 24, N = 6 for both conditions, *p* = 0.81, t.test). Box plots show 10, 25, 50, 75 and 90th percentiles with individual data points overlaid, means are shown as crosses as for (C). **(C)** The average intensity of the ribbons is comparable between PTXa control and mutant conditions (PTXa control: *n* = 327, PTXa mutant: *n* = 360; N = 9 in both conditions, *p* = 0.28, Mann-Whitney-Wilcoxon test).

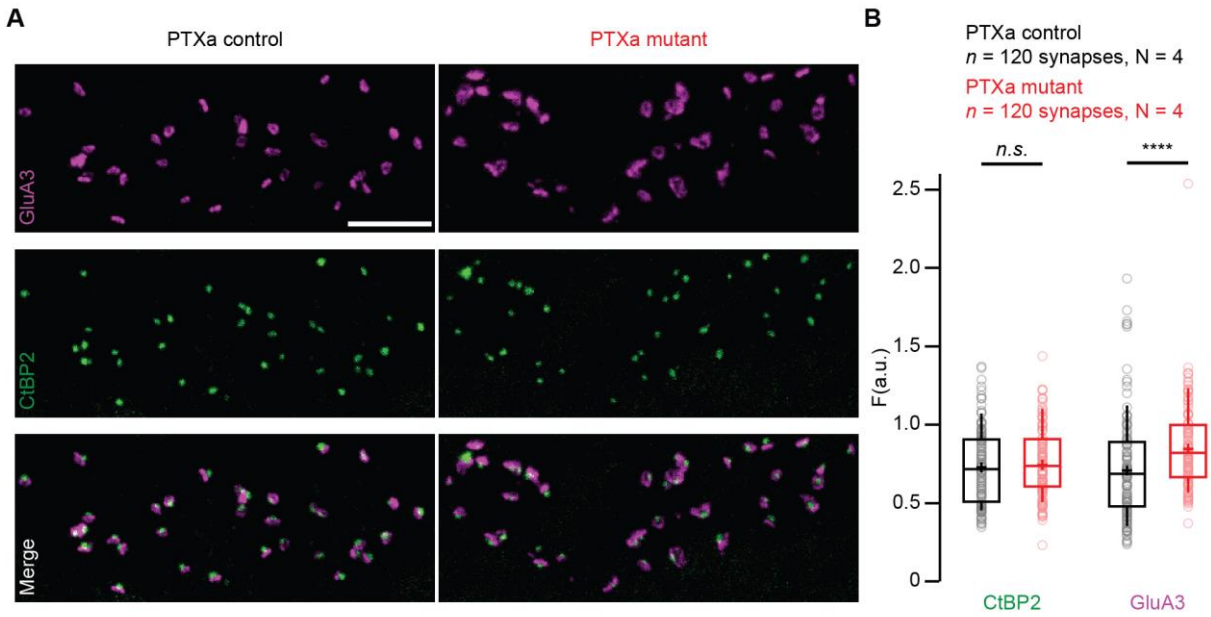

Fig. S3: PTXa expressing IHCs exhibit enlarged AMPAR clusters with preserved ring-like shape

(A) Maximum intensity projections of confocal sections from organs of Corti immunolabeled for GluA3 (magenta) and ribbon marker CtBP2 (green). Scale bar = 5 µm. **(B)** Mean intensities of the synaptic ribbons were unchanged but intensities of the postsynaptic GluA3 receptors were significantly increased in the PTXa mutant IHCs (red circles) as compared to PTXa control IHCs (black circles) (*n* = 120 synapses, N = 4 for both conditions, $p < 0.00001$, Mann-Whitney-Wilcoxon test for both conditions).

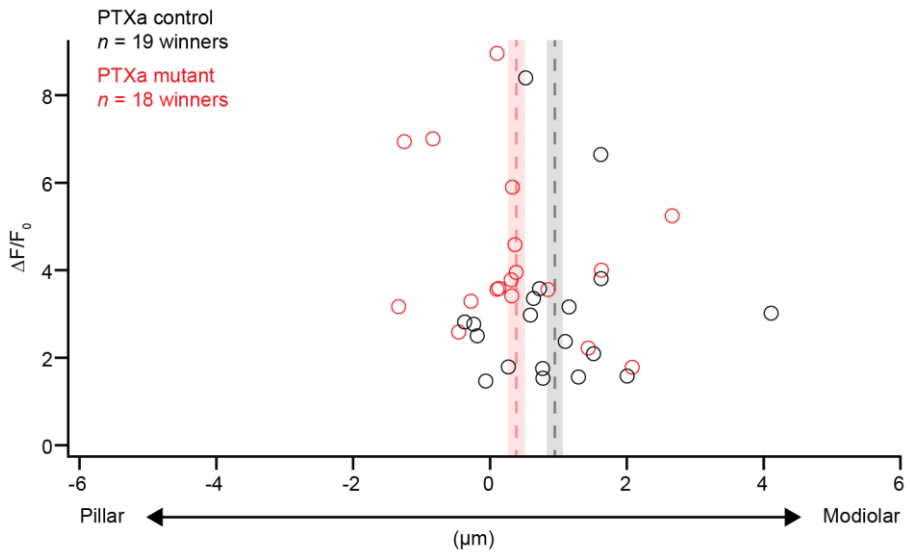

Fig. S4: Winning AZ Ca^{2+} influx strength along the pillar-modiolar axis

Maximal Ca^{2+} influx of the winning AZs (PTXa mutant in red, *n* = 18 winners vs. PTXa control in black, *n* = 19 winners) as a function of position along the pillar–modiolar axis. Mean (dashed line) ± S.E.M. (shaded areas) of their position did not differ significantly (*p* = 0.10, t.test)

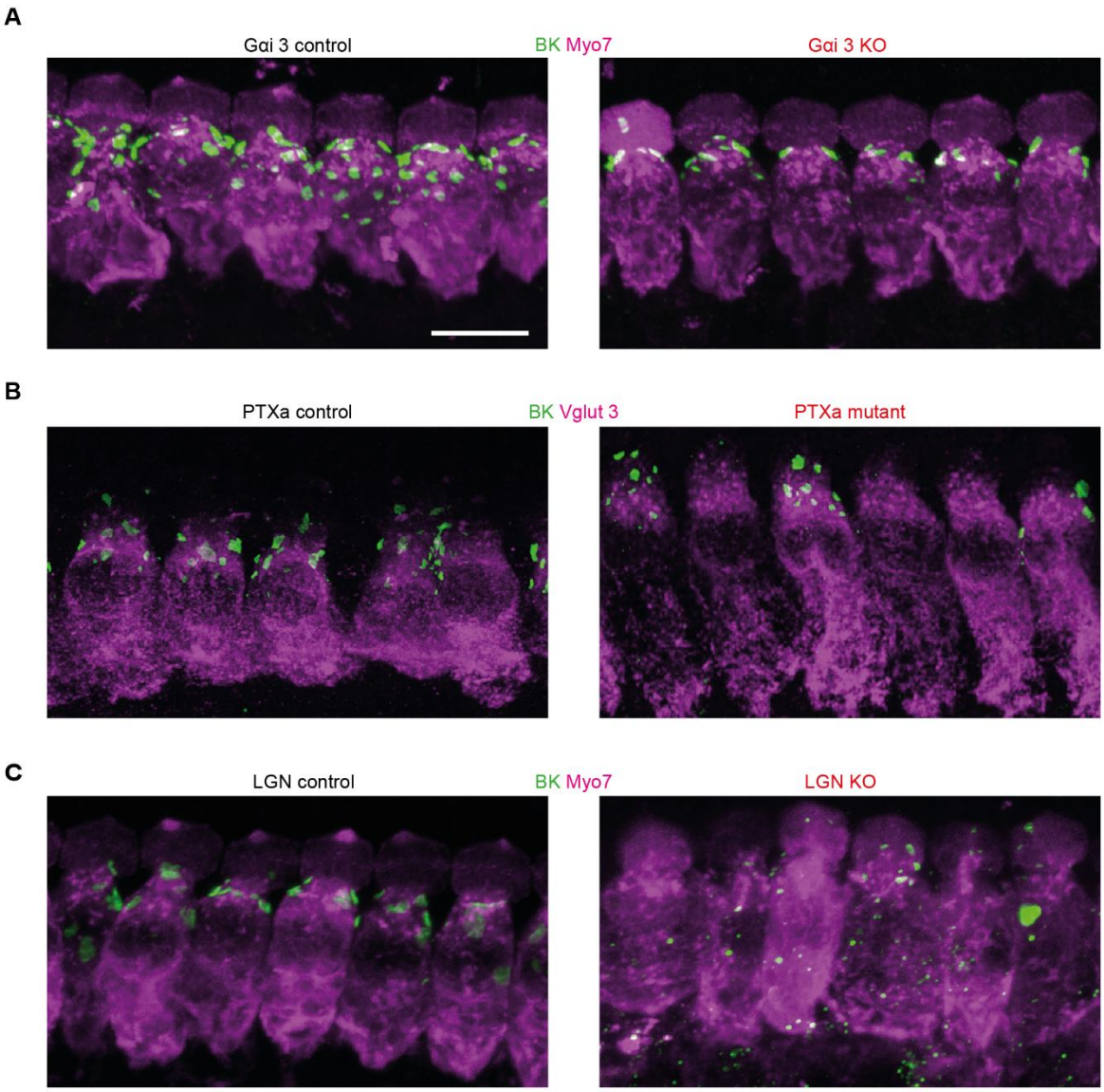

Fig. S5: Immunostaining study of BK channel clustering in *Gαi3*, PTXa and *LGN* mutant inner hair cells

(A) Maximal projection of confocal sections from organs of Corti co-immunolabeled for the large-conductance Ca^{2+} activated K^{+} (BK) channels (green as for B, C) and the HC marker Myo7 (magenta as for B and C). The BK positive spots are still present in the *Gαi 3* KO IHCs, but in smaller amount. Scale bar = 5 µm as for (B) and (C). **(B)** The BK channels are co-stained with the IHC marker Vglut3 and exhibit a mosaic expression in the PTXa mutant IHCs, showing normal clustering or being absent (no signal). **(C)** The BK channels are co-stained with the IHC marker Vglut3 and exhibit a mosaic BK-channel expression in the *LGN* mutant IHCs, showing normal clustering in some IHCs while no signal was detected in other IHCs.

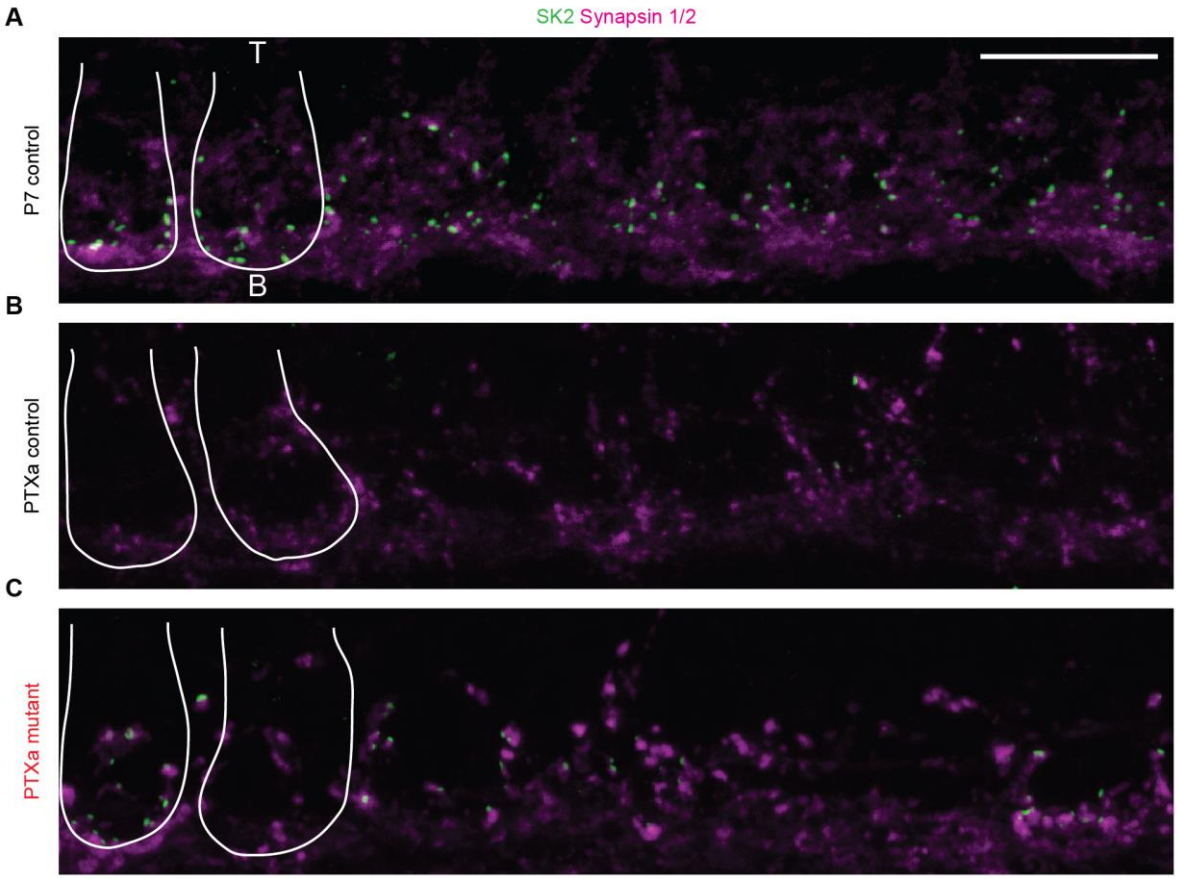

Fig. S6: SK2 channel clustering in PTXa mutant IHCs shows a mosaic phenotype

(A) Maximal projection of confocal sections from organs of Corti co-immunolabeled for the small-conductance Ca^{2+} activated K^+ (SK2) channels (green) and the efferent marker Synapsin 1/2 (magenta as for B, C): SK2 positive spots (likely clusters of SK2) are present in every immature P7 control IHC before hearing onset. The IHCs are delineated in white from bottom (letter B) to top (letter T). Scale bar = 10 µm as for (B, C). **(B)** The SK2 channels are almost completely absent in mature P22 littermate PTXa controls. **(C)** PTXa mutant P22 IHCs exhibit a mosaic expression of the SK2 channels with either normal clustering or no signal observed in a given IHC.

REFERENCES

1. Tarchini B, Jolicoeur C, Cayouette M (2013) A Molecular Blueprint at the Apical Surface Establishes Planar Asymmetry in Cochlear Hair Cells. *Dev Cell* 27(1):88–102.

2. Tarchini B, Tadenev ALD, Devanney N, Cayouette M (2016) A link between planar polarity and staircase-like bundle architecture in hair cells. *Development* 143(21):3926–3932.

3. Matei V, et al. (2005) Smaller inner ear sensory epithelia in Neurog 1 null mice are related to earlier hair cell cycle exit. *Dev Dyn Off Publ Am Assoc Anat* 234(3):633–650.

4. Jiang M, Spicher K, Boulay G, Wang Y, Birnbaumer L (2001) Most central nervous system D2 dopamine receptors are coupled to their effectors by Go. *Proc Natl Acad Sci* 98(6):3577–3582.

5. Moser T, Beutner D (2000) Kinetics of exocytosis and endocytosis at the cochlear inner hair cell afferent synapse of the mouse. *Proc Natl Acad Sci U S A* 97(2):883–888.

6. Lindau M, Neher E (1988) Patch-clamp techniques for time-resolved capacitance measurements in single cells. *Pflüg Arch Eur J Physiol* 411(2):137–146.

7. Sanchez del Rio M, Pareschi G (2001) Global optimization and reflectivity data fitting for x-ray multilayer mirrors by means of genetic algorithms. *SPIE Proc*:88–96.

8. Ohn T-L, et al. (2016) Hair cells use active zones with different voltage dependence of Ca2+ influx to decompose sounds into complementary neural codes. *Proc Natl Acad Sci* 113(32):201605737.